Journal Pre-proofs

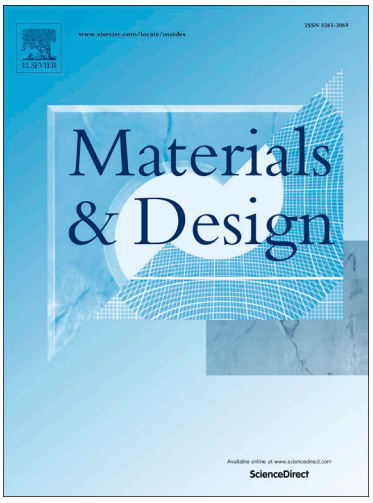


# Additive metal printing on multi materials using an atmospheric pressure plasma jet on a 5-Axis platform

Oliver S.J. Hagger, Michael A. Parkes, Francis Lockwood Estrin, Stefanos Agrotis, Ivan P. Parkin, Albertus D. Handoko, Daren J. Caruana

PII: S0264-1275(25)00101-7
DOI: https://doi.org/10.1016/j.matdes.2025.113681
Reference: JMADE 113681

To appear in: *Materials & Design*

Received Date: 20 November 2024
Revised Date: 23 January 2025
Accepted Date: 30 January 2025

Please cite this article as: Hagger, O.S.J., Parkes, M.A., Estrin, F.L., Agrotis, S., Parkin, I.P., Handoko, A.D., Caruana, D.J., Additive metal printing on multi materials using an atmospheric pressure plasma jet on a 5-Axis platform, *Materials & Design* (2025), doi: https://doi.org/10.1016/j.matdes.2025.113681

# Additive Metal Printing on Multi Materials using an Atmospheric Pressure Plasma Jet on a 5-Axis Platform

Oliver S. J. Hagger[a], Michael A. Parkes[a], Francis Lockwood Estrin[a], Stefanos Agrotis[a,b], Ivan P. Parkin[a], Albertus D. Handoko[b] and Daren J. Caruana*[a]

## Abstract

Post-production embellishment of objects with metal tracks presents challenges, due to the need for multiple processing steps and the complexity of navigating intricate substrate geometries. Here we describe a flexible approach to deposit conducting metal tracks on 3D objects using an atmospheric pressure plasma jet (APPJ). APPJs offer distinct advantages over traditional inkjet printing methods as they do not require metal particle inks or post-processing. An in-house-built APPJ print head was mounted onto a 5-axis platform to demonstrate metal printing on multifaceted metal, ceramic and glass complex objects. We use finite element modelling of the flow characteristics at the jet nozzle exit to understand and predict the track deposition. The modelling was corroborated through Schlieren imaging of the gas flow as well as chemical and physical characterisation of the resulting deposited track. Conductive metallic tracks of 0.3 mm widths were deposited on non-planar surfaces with one pass at a rate of 1 mm $s^{-1}$, using simple aqueous metal salts with an average plasma power of 10 W. Our findings reveal conductivity, adhesion strength and precision which present a benefit for additive manufacturing.

## Introduction

For many decades metal deposition has been a key feature of the electronics industry driven by the need to create progressively smaller features. Processes such as reductive physical vapour deposition (PVD)[1,2], chemical vapour deposition (CVD)[3] and electrodeposition[4] have been essential to fuel the advancement of electronic devices by depositing metal and dielectric materials with incredible precision. However, recently the emphasis has been reshaped towards developing more accessible deposition techniques, where feature size may not be the driver, instead the ability to deposit materials on a variety of substrates rapidly and with high adhesion. Here we introduce and demonstrate a metal printing method using an atmospheric pressure plasma jet (APPJ) capable of printing on multiple materials and 3D substrates in a single step.

Post-production metal printing is often done using inkjet printing, an established process with the capability to deposit metals[5] on multiple substrates[6–9] over a large scale at a low cost. However, inkjet printing has limitations, such as the requirement for pre-synthesised inks, and the need for a post-printing step to fully sinter the deposition. These limitations may prolong production time and increase the complexity of the process and cost. Ultimately, these limitations may affect the suitability of inkjet printing for certain applications, perhaps most importantly temperature-sensitive substrates that cannot withstand high curing temperatures.

*a. Department of Chemistry, Christopher Ingold laboratories, 20 Gordon St., London, WC1H 0AJ.*
*b. Institute of Materials Research and Engineering (IMRE), Agency for Science, Technology and Research (A*STAR), 2 Fusionopolis Way, Innovis #08-03, Singapore 138634, Republic of Singapore*

Atmospheric pressure plasma jets are an emerging promising avenue for precise and controlled metallic deposition processes without the need for post-processing.[10–17] The type of plasma used here is a non-equilibrium plasma containing highly energised electrons, but the ions and neutral species or atoms have a temperature just above room temperature. [18,19] As a result a plasma in contact with a surface transfers little heat energy. Sometimes referred to as cold plasmas, atmospheric pressure plasmas are used extensively to clean surfaces for adhesion promotion for bonding applications and in some cases chemical or physical modification of surfaces.[20] The unique chemical and physical properties of plasmas stem from the presence of free electrons which 'hoards' much of the energy used to form the stable self-sustaining plasma. Relevant to this present study, the presence of free electrons presents a realistic prospect of reducing metal salts to their respective zerovalent metal electrochemically. We have shown that plasma electrons are responsible for the reduction of copper oxide on a surface to copper. [17,21–27] Plasma deposition of zerovalent metal features has been reported by Alder et al.,[11] Gutierrez et al.,[12,13] and Manzi et al.,[14] with significant progress demonstrated in applications such as SERS surfaces, antennas, and consumer electronics. By atomising an aqueous solution of metal salt directly into the plasma gas feeding the APPJ, it is possible to deposit electrically conducting metal tracks in a single step on a variety of substrates ranging from glass to polymers.[17] Here we extend this deposition process on curved topologies using a 5-axis stage.

In this work, a 3D printer was modified by the addition of two further axes to create a 5-axis platform for enhanced design possibilities and material deposition techniques. Inspired by the pioneering work of Hong et al.[28,29] who described the conversion of a 3D printer to a 5-axis printer. Using a 5-axis printer instead of a 3-axis system provides distinct advantages, particularly the ability to deposit onto curved, uneven, or unconventional surfaces.

# Experimental

## 5-axis printer

The approach to create a 5-axis deposition system similar to Hong et al.,[28,29] was to modify a Prusa i3 MK3S with a Duet2 and Due5x expansion board (Duet3D) enabling the utilisation of 5-axis motion control axes. The original heated bed was replaced with a custom bed that accommodated the two additional movement axes, as illustrated in **Fig. 1(a, b).** All relevant components and design files can be found in the GitHub repository associated with Hong, F. et al.'s initial paper.[29]

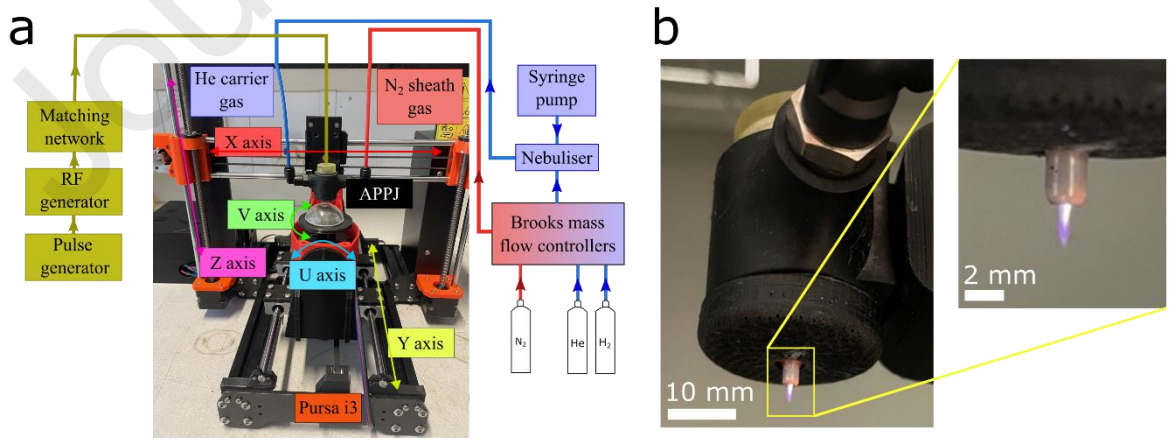


**Fig. 1** – APPJ set up. (a) Schematic setup of a modified Prusa i3 3D printer with the attachment of two additional axes (U and V) with APPJ mounted. (b) Ignited plasma plume extending from the end of the APPJ.

Modifications were implemented to enable the integration of an APPJ and facilitate metal deposition. Notably, the entire nozzle extruder was replaced with the APPJ via a simple 3D-printed component designed for magnetic attachment, as seen in **Fig. S1(a, b, c)**. The final APPJ setup is depicted in **Fig. 1(b) and Fig. S1(d).** All elements were created using Autodesk Fusion 360 and printed on a QIDI i-mate 3D printer using a range of print materials including polylactic acid (PLA) (RS Pro, UK) and polyethene terephthalate glycol (PET-G).

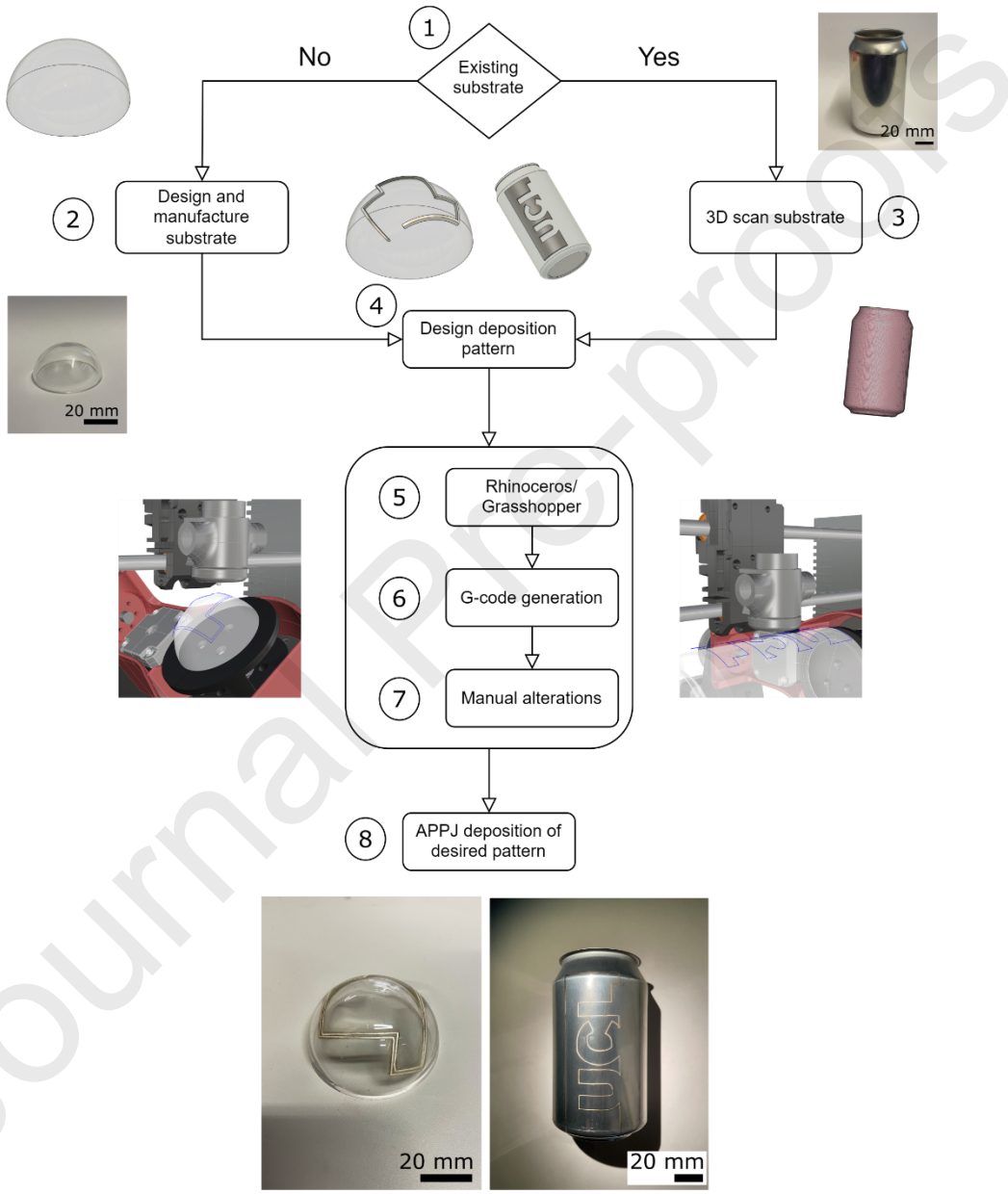


**Fig. 2** – Flow diagram depicting metallic deposition from start to finish. Depiction of the APPJ deposition process in 8 steps, based on whether the substrate already exists or needs to be manufactured first.

## Printing Approach

The process begins with one of two approaches, in **Fig. 2**, depending on whether the object already exists or is pending production. For models pending production, Case I taking the left route in **Fig. 2**, the CAD model is used to design the deposit on a substrate. If the model already exists, as shown in Case II, taking the right route (3) in **Fig. 2**, the item must be measured, and in our case, a 3D laser scanner is used to capture the topology of arbitrary surfaces on existing substrates. This high-resolution scanner can capture the intricate details of any surface with a 3D resolution of 0.2 mm and a point resolution of 0.1 mm. In collaboration with the Institute of Making, UCL, a comprehensive 3D scan (Artec Leo 3D laser scanner) of an aluminium beverage can was captured and used to design a CAD model upon which the design of the metal print was planned. This scanning procedure encompassed full 360-degree scans, enabling the capture of a volume up to 160,000 $cm^3$. Additionally, it features a real-time 3D reconstruction rate of up to 28 frames per second (fps), facilitated by the NVIDIA Jetson TX2 processor, allowing for instantaneous data compilation. 3D scanning technology remains nascent and, therefore, warrants additional refinement. The Artec Leo scanner encountered difficulties achieving absolute surface precision, requiring the implementation of techniques such as hole filling and surface smoothing within the Artec Studio 18 software. While proficient in scanning simple objects and surfaces, the software exhibited limitations in handling finer and more intricate surfaces.

The laser scans yielded rudimentary meshes, which were subsequently imported into the CAD software Fusion 360 for further exploration. However, imperfections may occur within the resulting tessellation from the 3D scan process. Consequently, while the mesh generated may suffice for straightforward scenarios, caution is warranted in more complex situations, where these scans should be utilised as guiding references rather than definitive representations.

## Design of Deposition Pattern

A simple 2D pattern was designed according to the deposition pattern. The patterns were reformed as functional 3D models. Leveraging Fusion 360's 'replace face' feature, the design was aligned with the curved surface of a glass hemisphere for the upper and lower face of the extruded object. The result was a fully rounded 3-dimensional extruded circuit drawing ready for export from CAD software. **Fig. S2(a, b)** show the hemisphere and modelled print placed on the 5-axis system.

## 5-axis slicing – Rhinoceros/Grasshopper

Rhinoceros 3D version 7, with Grasshopper integrated, was used for conformal slicing, G-code generation, and scripting. Grasshopper is a visual programming language integrated with Rhinoceros 3D that enables users to create parametric designs and automate workflows through a node-based interface. By manually selecting the substrate, the supportless structure and z-axis of the supportless structure G-code were generated in multiple axes. The supportless structure is the metallic deposition pattern designed in the previous Fusion CAD software. By also selecting the z-axis of the deposition pattern, the software can determine the top layer for efficient deposition. **Fig. S3(a)** depicts the proposed UCL motif for deposition. **Fig. S3(b, c, d, e)** shows the simulated movement of the 5-axis print.

Grasshopper parameters such as layer height, travel height, and travel speed can be easily modified for use with the APPJ. The G-code script underwent multiple refinements to accommodate the plasma printer, facilitating smooth metallic printing specifically altered x-direction movement, keeping the APPJ as static as possible. Any large movements of the APPJ would result in an increase in reflected power and loss of plasma jet plume stability.

## APPJ deposition

The APPJ deposited silver on unmodified substrates as follows. A solution of 5 x $10^{-3}$ M silver nitrate (99.9%, Thermo Scientific, UK) in deionised water (18 MΩ·cm, ELGA) was injected using a syringe pump (Harvard Apparatus, UK) at a rate of 0.5 mL $min^{-1}$ into a nebuliser. The nebuliser (Teledyne CETAC Technologies) atomised the solution and carried the nebuliser through a drying and cooling chamber operating at 120 °C and 0 °C, respectively. The dry silver nitrate's gas stream was then combined with helium (99.9+ %, BOC) 0.32 L $min^{-1}$ and hydrogen (99.9+ %, BOC) 10 mL $min^{-1}$ plasma gas and fed into the plasma jet assembly. Brooks mass flow controllers controlled all gas flow rates.

The plasma was ignited at a stainless-steel needle electrode tip in a 440 μm I.D. ceramic nozzle. A CESAR 136 radio frequency (RF) generator (Advanced Energy, US) operating at 13.56 MHz was used to drive the plasma at a single electrode jet. The RF driving signal was pulse width moderated at 18 kHz, giving plasma average power of 10 W and passed through a matching network consisting of a variable inductor to match the 50 Ω output impedance of the RF generator. The plasma exited the ceramic nozzle to form a stable plume extending 8 mm beyond the tip orifice. A nitrogen sheath gas, 1.5 L $min^{-1}$, surrounded the plume to reduce air entrainment and aid plasma stability; this setup was previously described in Lockwood Estrin et al.[17]

## CFD modelling

Computation fluid dynamic modelling was carried out using axisymmetric modelling of the APPJ using ANSYS 2021 (ANSYS Inc., US). Design modeller was used to accurately model the jet, with ANSYS mesh software used to create a high resolution 25 μm mesh. Helium gas was simulated to flow through the jet while releasing discrete packets of silver particles ranging from 10 nm to 1 μm in diameter. The particles adhered to the Cunningham-corrected Stokes-Cunningham drag law, and Ranz-Marshall heat transfer coefficient, and considered Brownian Motion. The boundary conditions were configured to reflect the experimental conditions, aside from the bottom wall set to “trap” and the outlet set to “escape” at an atmospheric pressure of 101 325 Pa. Each calculation underwent 10,000 iterations, and records were analysed for velocity, pressure, and particle final positions.

## SEM

For surface and morphology analysis, high-resolution scanning electron microscopy was used. Images were obtained with a JSM 6701 and 7600 field emission SEM (JEOL, Japan) at an accelerating voltage of 10 kV. Non-conducting samples were coated with gold to aid charge dissipation during imaging. Particle size analysis from SEM images was carried out using ‘ImageJ’ software version 1.53 k to estimate the particle size distribution.[30]

## Optical

A VHX-7000 digital microscope (Keyence Corporation, Osaka, Japan), equipped with a Z20 (20–6000 x) objective (Keyence Corporation, Osaka, Japan) was used for all optical microscopy. Due to the size of the printed object SEM was not possible, therefore, 3D optical microscopy was used to measure the width of tracks on all substrates. Detailed SEM images of the tracks can be found in Lockwood Estrin et al.[17] The VHX-7000 digital microscope features a 1/1.7-inch, 12.22-megapixel CMOS sensor, offering resolutions of up to 4000 × 3000 pixels in 4K mode. For track width measurements images taken at 200 x or 400 x magnification was used giving a minimum vertical field of view of 1.14 mm or 0.570 mm respectively, provided good accuracy and high precision.

### TEM

To achieve highly magnified images of the metal particulates expelled from the APPJ during deposition, Transmission Electron Microscopy (TEM) was employed. The particles were carefully collected from the APPJ and deposited onto a TEM grid. For analysis, ultra-thin carbon support film (3 mm thick) mounted on lacey carbon grids from Agar Scientific was utilised. The analysis of the particles was carried out using a JEM-2100 electron microscope (JEOL, Japan).

### XPS

A Thermo K-Alpha photoelectron spectroscopy system (Thermofischer, US) equipped with a monochromatic Al-Kα (1486.6 eV) X-ray source was used for X-ray photoelectron and Auger electron spectra acquisition. Unless noted otherwise, spectra were collected from a spot of 50 µm diameter on the sample surface at a pass energy of 50 eV. Photoelectron energy offsets were minimised using an electron flood gun source during XPS spectra acquisition. Adventitious carbon C 1s peak at 284.8 eV was used as an internal energy calibration as needed. For the analysis of zerovalent silver, the top layer was ion-etched to remove any silver oxide that may have formed due to exposure to the atmosphere.

### PXRD

An Empyrean Grazing Incident Powder X-Ray Diffractometer from Malvern Panalytical was employed to acquire all diffraction patterns for the thin films discussed in this report. Unless specified otherwise, the 2θ range utilised ranged from 5° to 80°. The scan step size was set at 0.05, 0.5 times per step. Each experiment utilised a 40 kV generator voltage and a 40 mA tube current. The divergence slit was maintained at 0.38 mm and a fixed 0.1 receiving slit was utilised to generate the XRD patterns.

### AFM

A Keysight 5500 Atomic Force Microscopy instrument was used to measure and image the surface topology. Multi75Al-G silicon AFM cantilevers were purchased from Apex Probes. The AFM tip specifications are as follows, tip height 17 µm, tip set back 15 µm, tip radius <10 nm and half cone angle 20 ° - 25 °. Images were taken over a 5 µm × 5 µm area, with root-mean-square (RMS) roughness value determined by WSxM 5.0 software.

## Results and Discussion

### Case I: Printing onto a glass Hemisphere

The glass object, in this case, a hemisphere, was made to precise specifications according to a CAD model. It was securely attached to the printer's U-axis to ensure the plasma jet tip was 2 mm away at every point on the hemisphere, as shown in **Fig. 3(a)**. As the hemisphere was rotated and moved through a preprogrammed pattern, the plasma jet deposited silver metal on the surface of the glass. The final deposited track is shown in **Fig. 3(b to g), Fig. S4(a) and Fig. S4(b).** The tracks are formed by two consecutive passes and washed with deionised water to remove unreduced silver nitrate crystals from overspray. The overall deposition process took 240 s to complete the circuit (120 s to complete each pass). The track width was 300 µm size, two tracks were printed with a roughly 600 µm separation distance.

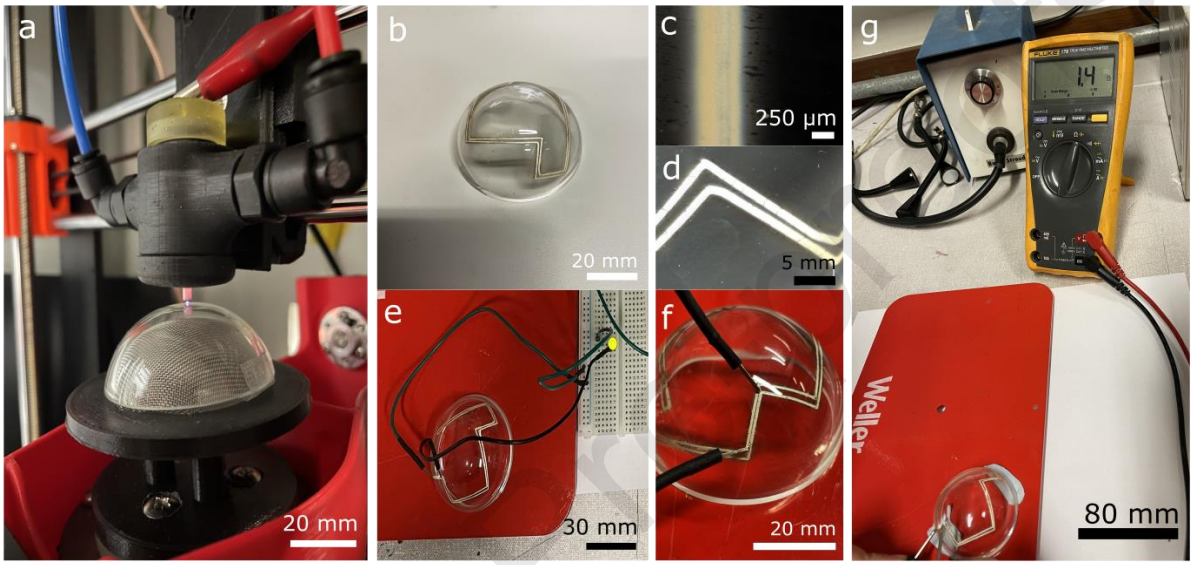


**Fig. 3**. Plasma jet deposition on a hemisphere. (a) Photographs of a glass hemisphere (radius 25 mm) mounted on the 5-axis platform with a metallic mesh positioned underneath the glass hemisphere held at an angle, showing the plasma jet deposition in progress. (b) The final print of conductive silver trace on the glass hemisphere substrate. (c, d) Magnified optical image of the silver track. (e) Optical image displaying an electrical circuit using Ag metal-deposited tracks as conductive components. (f) Magnified view of the conductive track connection. (g) Image showing conductance of silver metallic tracks on a glass hemisphere with the associated resistance measured using a two probe.

The chemical and physical characteristics of the silver deposit were investigated to confirm the oxidation state using XPS and XRD and the surface morphology using microscopy. The plasma was indeed able to reduce the metal salt to zerovalent metal, as demonstrated by the carbon-corrected XPS spectra, which were used to identify the Auger peaks, as shown in **Fig. 4(a)**. The spectra also show no silver oxide peaks, confirming the production of virtually pure zerovalent metal. XRD analysis further supports this by displaying the characteristic peaks of the FCC crystal pattern of silver metal, as illustrated in **Fig. 4(b)**. SEM analysis revealed that the deposit consists of small metal particles formed in the plasma jet, which then land on the surface to create a solid metal track, as shown in **Fig. 4(c)**. Particle size analysis from the SEM images indicates a mean particle size of approximately 48.06 nm with a spread of ± 11 nm shown in **Fig. 4(d**), consistent with TEM analysis depicted in **Fig. 4(e)**. AFM analysis of identical deposition on a planar surface, shown in **Fig. 4(f),** further demonstrates the size variation of the particles, revealing an RMS roughness value of 68 nm, indicative of a relatively flat surface topology with nanoscale peaks and troughs.

In addition to electrochemical reduction of the metal salt to zerovalent metal, the plasma also pretreats the surface which promotes the adhesion of the metal to the substrate. Plasma jets are used

extensively in industry to promote adhesion.[31] Physical changes are mainly to remove surface contaminants such as hydrocarbons, whilst the chemical changes that lead to changes in water contact angle or wettability. On glass, and other materials, the adhesion strength appears to be directly proportional to the extent of wettability of the surface to water. Plasma contains metastable species such as reactive radicals, electrons and ions, which can react with the pendent groups on the glass surface to promote the formation of hydrophilic functional groups such as hydroxides, aldehydes and acid groups. These all contribute to an increase in wettability, and thus promotion of adhesion. Li et al. [32] used molecular dynamics (MD) simulations to understand the wettability of surfaces with various groups and surface group density. They found the influence of aldehydes, acid and amino groups have a more dominate role compared to hydroxyl groups. Intuitively, the higher the functional group density on the surface the more hydrophilic the surface becomes. We believe both of these two factors contribute to the high adherence of the glass (or alumina) surface to the metal. We have investigated the strength of adherence using a stylus scratch test and discussed in ref. [18]. In this case track adherence was assessed using a Scotch tape® test. No visible difference was observed between the tracks before and after tape removal, even when repeated ten times. There was no discernible silver lifted on the tape and no change in the conductance of the track. Notably, no pre- or post-surface treatment was employed to achieve this level of adhesion. Whilst this test was rudimentary, the adhesion of silver tracks deposited on flat glass surfaces under identical conditions was extensively tested using a stylus scratch test and described in reference showcasing a similar result. [17].

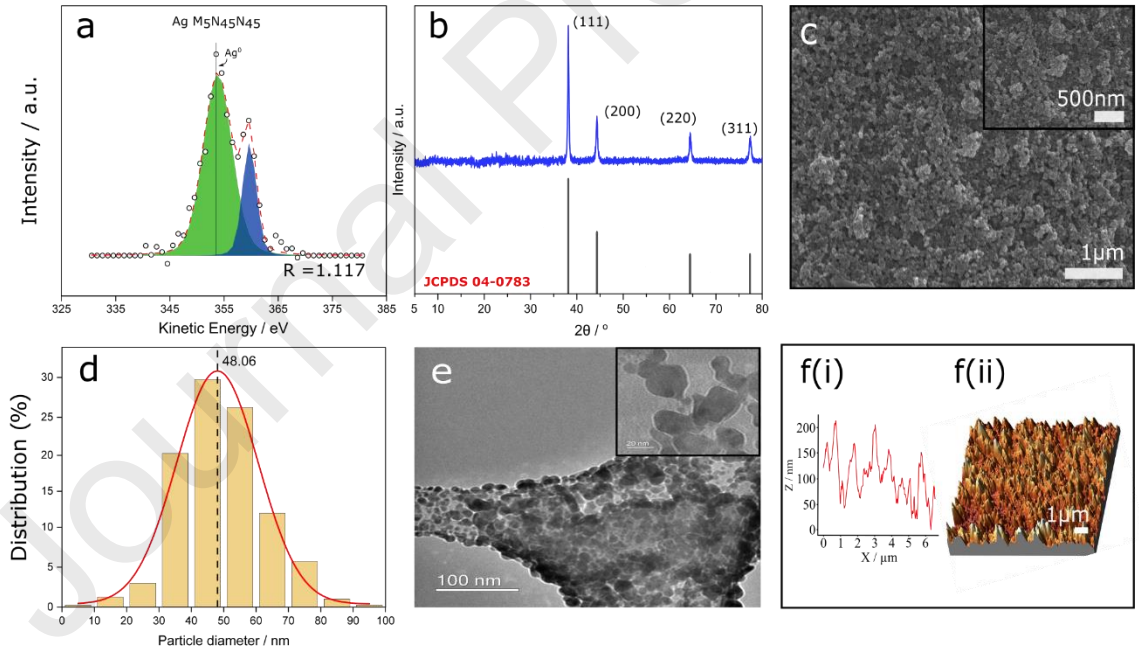


**Fig. 4.** Silver deposition analysis. (a) The XPS peaks were fitted with Lorentzian peak shape with an asymmetry parameter of 1.7, no Gaussian broadening, and Shirley background corrected. The spectra confirm the presence of pure zerovalent silver ($Ag^0$) at KE 358 eV with no detectable silver oxide peaks below the top layer. (b) XRD confirms the presence of silver FCC structure, in correspondence with JCPDS 04-0783. (c) SEM image APPJ Ag deposit, and (d) corresponding particle size distribution for the deposit. (e) TEM image of the Ag deposit showing particle structure. (f(i), f(ii)) AFM image of surface topology with inflated z-axis highlighting peaks and troughs.

The width of the deposited metal track depends on multiple factors including jet orifice diameter and helium flow rate. A computational fluid dynamic (CFD) model of the jet exit and substrate was used to

investigate the various dependencies of each variable on the width of the metal track. As described above, zerovalent metal particles are generated within the plasma jet in a range of diameters. These particles exit the jet and land on the surface beneath the orifice of the jet. The particles impact the surface depending on the particles' velocity mass and diameter. The 2D axisymmetric models of the gas velocity within the nozzle and at the exit as it impinges on the substrate are shown in **Fig. 5(a)**. The flow of gas out of the nozzle is laminar with maximum exit velocities of 389 and 207 m $s^{-1}$ determined for the 400 and 600 µm nozzles, respectively. Schlieren imaging of the gas flow also supports laminar flow of the helium gas exiting the nozzle, **Fig. 5(b)**.[33] Additional simulations for different flow rates through a 440 µm nozzle have an effect on the deposition stream in **Fig. S5(a, b).**

To simulate the particles landing on the substrate, 400 particles with a range of diameters from 10 nm to 1 µm were added to the plasma gas flow exiting the nozzle. The most probable landing zone for each size range was determined for two different nozzle sizes, 400 and 600 µm, with 300 mL $min^{-1}$ helium flow. The landing probability as a function of position is represented in **Fig. 5(c, d)** for the two different nozzle diameters in each particle size range. At the centre, at position zero, there is a low probability of any particles landing. This is due to the flow field of the helium jet, which is typical of a wall jet flow, creating a stationary zone directly beneath the centre of the nozzle. As a result, the probability of particles landing on the surface at this point is very low. For particles with a diameter of 1 µm or smaller, the particle's inertia is sufficient to be deflected and land at a set distance from the stationary zone, as described in **Fig. 5(c(i), d(i)).** With a 400 µm nozzle size, the spread of particles extends a shorter distance from the centre, creating a narrower track compared to the track deposited with a nozzle diameter of 600 µm. These simulations are mirrored in the actual profile of the resulting track as displayed in **Fig. 5 (c(ii), d(ii)),** for 400 and 600 µm, respectively. The track produced by the 400 µm nozzle shows a gap in the centre of the track, whereas the track produced by the 600 µm nozzle is more uniform. It's important to note that these simulations do not consider the effect of

plasma, which would increase carrier gas turbulence; however, the landing probabilities for the size ranges described here remain appropriate.[34]

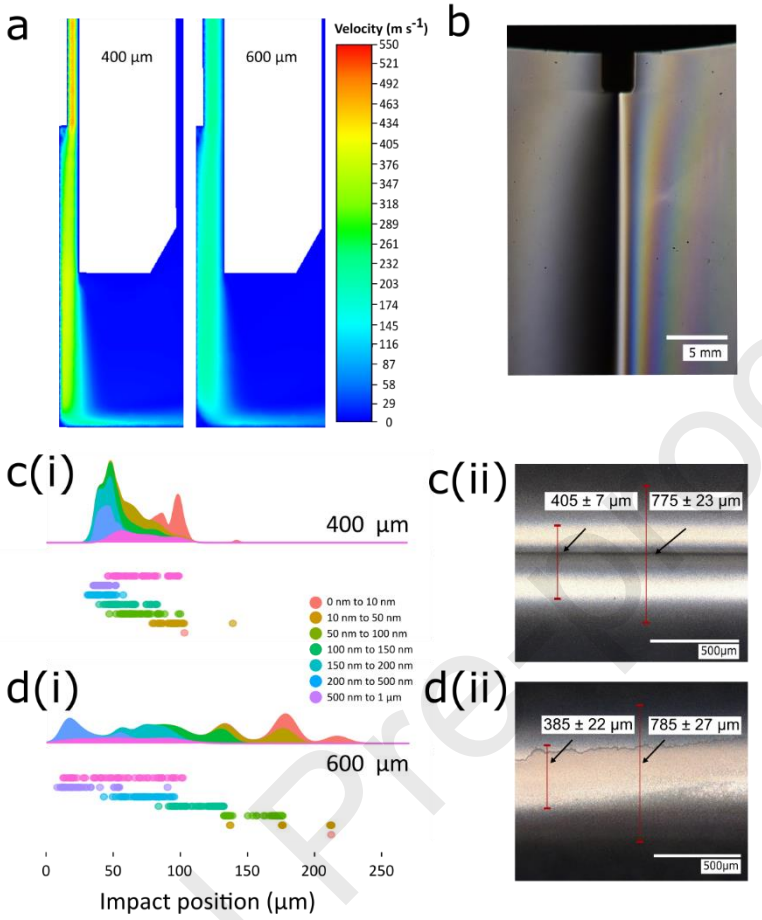


**Fig 5.** CFD simulations of APPJ. (a) ANSYS simulations of helium velocity flow through the jet with a 400 and 600 µm nozzle. (b) Schlieren imaging of laminar flow through the jet. (ci, di) Simulation of inert silver particles landing probability as a function of position relative to the centre of the nozzle. (cii, dii) Optical microscopy image of silver track deposited on glass for a single pass using 400 and 600 µm nozzle diameters at 200 x magnification, error stated is the standard deviation from five independent measurements.

The deposited circuit demonstrates a good level of conductivity that was greater than 40% of bulk silver conductivity. Two-point conductivity measurements of the metal tracks on a curved surface yielded a resistance of 1.4 Ω, displayed in **Fig. 3(g)**. Similar measurements were conducted on planar surfaces using a four-point probe, and the conductivity of silver produced via this identical APPJ process, as discussed in more detail by Lockwood Estrin, et al.[17], was 32 ± 5 x $10^6$ S $m^{-1}$, or greater than 40 % of bulk silver conductivity. **Fig. 3(g)** illustrates the measurement of the conductivity over a short distance. The conductivity was tested on a dielectric (glass hemisphere) hence the conductance was solely due to the metallic track.

## Case IIa: Deposition on a Scanned Drinks Can

Deposition was demonstrated on an existing object with no available CAD model, as an example we used a drinks can. To further validate the breadth of substrate APPJ can deposit on, a drinks can was chosen to demonstrate that being metallic the plasma which couples to the deposition surface can

also result in a silver metal deposit. The deposition design chosen was the UCL logo and a butterfly motif, along with other motifs described in **Fig. 6(b, c) and Fig. S6(a, b)**. Once the drinks can was scanned and mounted on the 5-axis printer, the print path was simulated for calibration purposes prior to metal printing by replacing the APPJ print head with a permanent marker. After this calibration, the metal printing was carried out under the same conditions as described for the glass hemisphere. The deposit had similar chemical and physical characteristics, although it was difficult to decouple the conductivity from the substrate contribution in this case. The adhesion was tested using the Scotch tape® method, no silver metal on the tape was visible by eye, even when repeated ten times. It is expected that the mechanism for adhesion promotion as discussed above for glass also applies for aluminium oxide. In fact the wettability on the surface of aluminium and its alloys is increased after plasma exposure for adhesion promotion of various materials, as reviewed by Patel and Bhowmik[27].

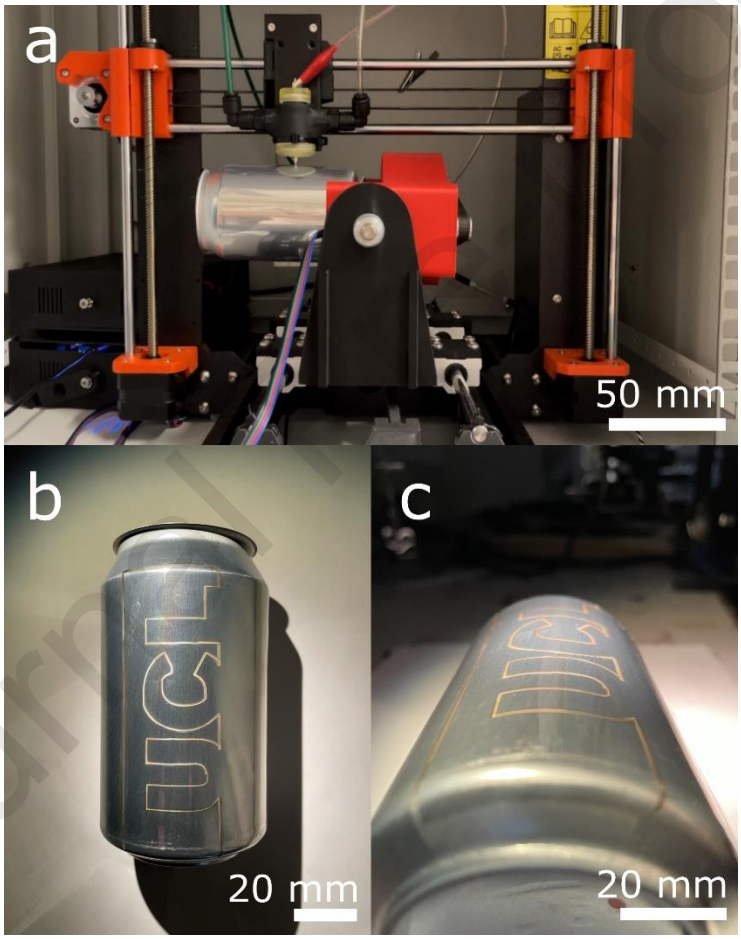


**Fig. 6.** APPJ situated on 5-axis instrument. (a) Plasma deposition of the metallic track during operation. (b, c) Final UCL motif deposition on aluminium beverage can using an APPJ.

## Case IIb: Deposition on Scanned Ceramic Object

Our methodology demonstrates versatility in depositing on a diverse range of materials. Notably, alumina, a white oxide of aluminium, can be effectively decorated with adherent metal tracks using an APPJ coupled with our custom-modified 5-axis printer. Unlike the drinks can, the ceramic surface did

not require pre-treatment with white matte spray due to its non-reflective nature. Utilising an Artec Leo laser 3D scanner comprehensively to scan a ceramic alumina crucible, as shown in **Fig. S7**. The ceramic crucible was mounted on the 5-axis printer, and the design of the metallic track was generated and simulated with G-code before printing, as displayed in **Fig. S8**. The APPJ deposition speed was 1 mm $s^{-1}$, using a silver nitrate concentration of 5 mM and a helium flow of 300 mL $min^{-1}$, with 3 % hydrogen to aid reduction to zerovalent silver. The plasma deposition was aided with a nitrogen curtain gas to stop oxidation from the atmosphere. The forward power used for the deposition was 19 W with a 50 % duty cycle operating at 18 kHz. The deposition on the ceramic crucible resulted from a single pass of plasma deposition, resulting in a conducting track deposited as shown in **Fig. 7(a).**

The resultant track has a width of roughly 230 ± 12 µm and an outer 'spray' track of 470 ± 9 µm, as displayed in **Fig. 7(b, c and d)**. Only the inner track was conducting; the jet's overspray was not conducting. The properties of the substrate material require some refinement of the printing variables to ensure the metal track adheres to the surface with a defined track width and conductivity. The versatility of patterns, substrate, and deposition material is broad, and these patterns and materials were chosen to showcase the technique's flexibility.

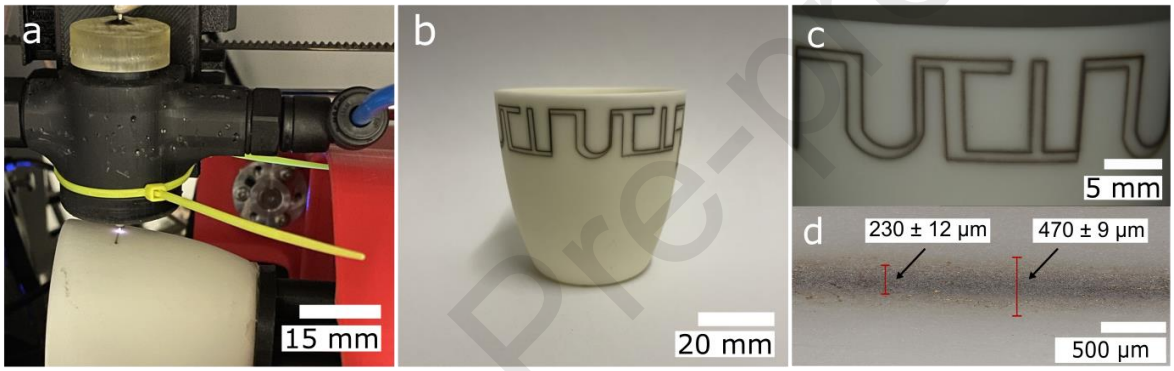


**Fig. 7.** Metallic deposition on ceramic crucible. (a) Real-time APPJ deposition of zerovalent silver track using the 5-axis system. (b) Final metallic track deposition on alumina crucible. (c & d) Optical microscopy image displaying the deposited metallic track on ceramic close-up high-resolution images displaying track width, at 400 x magnification, error stated is the standard deviation from five independent measurements.

## Conclusion

In conclusion, this study has demonstrated the capabilities of the APPJ metal track.[17] The method utilises previously published methods of using a modified Pursa i3 MKS3, adding two additional axes to the original instrument as described by Hong et al.[28,29] Harnessing the potential of a 5-axis printer, in contrast to the conventional 3-axis counterpart, has showcased the following advantages: (1) the ability to deposit conducting tracks onto complex, curved, (2) no pre or post-processing is required, (3) metal particle-free ink, and (4) no complex synthetic steps for the ink.

Through the integration of Fusion 360 and Rhinoceros 7 CAD software, intricate designs were seamlessly transformed into practical, tangible models. The collaboration between design and technology has led to the successful deposition of conductive metallic tracks, showcasing the potential for precise and efficient printing on challenging substrates. The refined techniques, including integrating Grasshopper for multi-dimensional G-code generation, have opened doors for intricate and precise depositions.

The technique of plasma-deposited metallic tracks on various substrates, either planar or topologically challenging, has been demonstrated. The combination of quick and simple technique of scanning a rudimentary object, simulating and manufacturing the tangible conductive metallic tracks, is an

accessible example of additive manufacturing. This work demonstrates significant advantages over traditional metallic inkjet printing [11-16], providing a simpler yet more versatile technique for depositing multiple metals on non-planar surfaces. It enables deposition on temperature-sensitive and challenging materials, with no need for post-processing or sintering. This study quantifies the one-step deposition of zero-valent metals, verified by XPS spectra. The deposited sliver metal tracks show a level of conductivity that was greater than 40% of bulk silver conductivity. From two-point conductivity measurements of the metal tracks on a curved surface yielded a resistance of 1.4 Ω. Furthermore, the resulting metallic particles measure an average diameter of 48.0 nm, forming track lines approximately 230 µm wide using a 400 µm nozzle. Simulations with varying nozzle sizes and velocities were conducted to optimise deposition further.

Overall, this work underscores the power of innovation in material deposition, bridging the gap between design and fabrication. As this technology continues to evolve, it promises to shape industries ranging from electronics to art conservation and beyond, offering a promising future for precision deposition on diverse and challenging surfaces. The successful use of these instruments highlights the immense potential of 5-axis deposition as a transformative tool in additive manufacturing.

## Author Contributions

Conceptualisation: OSJH, DJC

Methodology: OSJH, DJC

Investigation: OSJH, MAP, FLE, SA

Visualisation: OSJH

Formal analysis: OSJH

Project administration: OSJH

Supervision: IK, IPP, DJC

Writing – original draft: OSJH, DJC

Writing – review & editing: IPP, MAP

## Conflicts of Interest

There are no conflicts of interest to declare.

## Acknowledgements

OSJH wishes to thank EPSRC and Dstl for an ICASE. We thank John Crawley for producing the Borosilicate glass hemisphere and Andy Stewart for assistance with the Keyence microscope. The authors wish to thank Dr Ellie Doney at the Institution of Making, UCL, for assistance with the object scanning. This work was also supported by EPSRC project EP/T024836/1.

## References

[1] G. Skordaris, K.D. Bouzakis, T. Kotsanis, P. Charalampous, E. Bouzakis, O. Lemmer, S. Bolz, Film thickness effect on mechanical properties and milling performance of nano-structured multilayer PVD coated tools, Surf Coat Technol 307 (2016) 452–460. https://doi.org/10.1016/J.SURFCOAT.2016.09.026.

[2] A. Baptista, F.J.G. Silva, J. Porteiro, J.L. Míguez, G. Pinto, L. Fernandes, On the Physical Vapour Deposition (PVD): Evolution of Magnetron Sputtering Processes for Industrial Applications, Procedia Manuf 17 (2018) 746–757. https://doi.org/10.1016/J.PROMFG.2018.10.125.

[3] K.L. Choy, Chemical vapour deposition of coatings, Prog Mater Sci 48 (2003) 57–170. https://doi.org/10.1016/S0079-6425(01)00009-3.

[4] G. Zangari, Electrodeposition of Alloys and Compounds in the Era of Microelectronics and Energy Conversion Technology, Coatings 5 (2015) 195–218. https://doi.org/10.3390/COATINGS5020195.

[5] A. Kamyshny, J. Steinke, S. Magdassi, Metal-based Inkjet Inks for Printed Electronics, The Open Applied Physics Journal 4 (2011) 19–36. https://doi.org/10.2174/1874183501104010019.

[6] S. Conti, L. Pimpolari, G. Calabrese, R. Worsley, S. Majee, D.K. Polyushkin, M. Paur, S. Pace, D.H. Keum, F. Fabbri, G. Iannaccone, M. Macucci, C. Coletti, T. Mueller, C. Casiraghi, G. Fiori, Low-voltage 2D materials-based printed field-effect transistors for integrated digital and analog electronics on paper, Nat Commun 11 (2020) 1–9. https://doi.org/10.1038/s41467-020-17297-z.

[7] X. Nie, H. Wang, J. Zou, Inkjet printing of silver citrate conductive ink on PET substrate, Appl Surf Sci 261 (2012) 554–560. https://doi.org/10.1016/J.APSUSC.2012.08.054.

[8] S.G. Kirtania, M.A. Riheen, S.U. Kim, K. Sekhar, A. Wisniewska, P.K. Sekhar, Inkjet Printing on a New Flexible Ceramic Substrate for Internet of Things (IoT) Applications, Micromachines (Basel) 11 (2020) 841. https://doi.org/10.3390/MI11090841.

[9] Y. Yu, J. Zhang, J. Liu, Biomedical Implementation of Liquid Metal Ink as Drawable ECG Electrode and Skin Circuit, PLoS One 8 (2013) e58771. https://doi.org/10.1371/JOURNAL.PONE.0058771.

[10] O.S.J. Hagger, M.E. Sener, I. Khan, F.L. Estrin, S. Agrotis, A.D. Handoko, I.P. Parkin, D.J. Caruana, Rapid single step atmospheric pressure plasma jet deposition of a SERS active surface, Mater Adv 4 (2023) 3239–3245. https://doi.org/10.1039/D3MA00249G.

[11] R. Alder, J. Hong, E. Chow, J. Fang, F. Isa, B. Ashford, C. Comte, A. Bendavid, L. Xiao, K.K. Ostrikov, S. Fu, A.B. Murphy, Application of Plasma-Printed Paper-Based SERS Substrate for Cocaine Detection, Sensors 21 (2021) 810. https://doi.org/10.3390/S21030810.

[12] D.H. Gutierrez, P. Doshi, D. Nordlund, R.P. Gandhiraman, Plasma jet printing of metallic patterns in zero gravity, Flexible and Printed Electronics 7 (2022) 025016. https://doi.org/10.1088/2058-8585/AC73CB.

[13] D.H. Gutierrez, R. Bhattacharya, P. Doshi, D. Nordlund, R.P. Gandhiraman, Plasma jet printing of copper and silver antennas operating at 2.4 GHz, J Electromagn Waves Appl 38 (2024) 790–801. https://doi.org/10.1080/09205071.2024.2336033.

[14] J. Manzi, T. Varghese, J. Eixenberger, L. Prakasan, D. Estrada, H. Subbaraman, One-Step Plasma Jet Deposition and Self-Sintering of Gold Nanoparticle Inks on Low-Temperature Substrates, IEEE Journal on Flexible Electronics 3 (2024) 197–204. https://doi.org/10.1109/JFLEX.2024.3399710.

[15] J. Manzi, N. Kandadai, R.P. Gandhiraman, H. Subbaraman, Plasma Jet Printing: An Introduction, IEEE Trans Electron Devices 70 (2023) 1548–1553. https://doi.org/10.1109/TED.2023.3248526.

[16] V.A. Tran, T.T.V. Tran, V.T. Le, V.D. Doan, G.N.L. Vo, V.H. Tran, H. Jeong, T.T.T. Vo, Advanced nano engineering of surface-enhanced Raman scattering technologies for sensing applications, Appl Mater Today 38 (2024) 102217. https://doi.org/10.1016/J.APMT.2024.102217.

[17] F. Lockwood Estrin, O.S.J. Hagger, M.E. Sener, D.J. Caruana, Metal Painting by Plasma Jet, Adv Mater Interfaces (2024) 2400256. https://doi.org/10.1002/ADMI.202400256.

[18] I.J. Kang, C.H. Cho, H. Chang, S.O. Jang, H.J. Park, D.G. Kim, K.M. Lee, J.H. Kim, Characteristics of Plasma Flow for Microwave Plasma Assisted Aerosol Deposition, Nanomaterials 11 (2021) 1705. https://doi.org/10.3390/NANO11071705.

[19] P.J. Bruggeman, F. Iza, R. Brandenburg, Foundations of atmospheric pressure non-equilibrium plasmas, Plasma Sources Sci Technol 26 (2017) 123002. https://doi.org/10.1088/1361-6595/AA97AF.

[20] A. Van Deynse, P. Cools, C. Leys, R. Morent, N. De Geyter, Surface modification of polyethylene in an argon atmospheric pressure plasma jet, Surf Coat Technol 276 (2015) 384–390. https://doi.org/10.1016/J.SURFCOAT.2015.06.041.

[21] J. De Backer, J. Razzokov, D. Hammerschmid, C. Mensch, Z. Hafideddine, N. Kumar, G. van Raemdonck, M. Yusupov, S. Van Doorslaer, C. Johannessen, F. Sobott, A. Bogaerts, S. Dewilde, The effect of reactive oxygen and nitrogen species on the structure of cytoglobin: A potential tumor suppressor, Redox Biol 19 (2018) 1–10. https://doi.org/10.1016/J.REDOX.2018.07.019.

[22] L.M. Wallenhorst, L. Loewenthal, G. Avramidis, C. Gerhard, H. Militz, G. Ohms, W. Viöl, Topographic, optical and chemical properties of zinc particle coatings deposited by means of atmospheric pressure plasma, Appl Surf Sci 410 (2017) 485–493. https://doi.org/10.1016/J.APSUSC.2017.03.021.

[23] G.T. Bae, H.J. Jang, E.Y. Jung, Y.R. Lee, C.S. Park, J.Y. Kim, H.S. Tae, Development of an Atmospheric Pressure Plasma Jet Device Using Four-Bore Tubing and Its Applications of In-Liquid Material Decomposition and Solution Plasma Polymerization, Polymers (Basel) 14 (2022) 4917. https://doi.org/10.3390/POLYM14224917.

[24] S. Agrotis, M. Emre Sener, O.S.J. Hagger, A.D. Handoko, D.J. Caruana, One-Step synthesis of nanosized Cu-Ag films using atmospheric pressure plasma jet, Appl Mater Today 39 (2024) 102286. https://doi.org/10.1016/J.APMT.2024.102286.

[25] M.E. Sener, D.J. Caruana, Modulation of copper(I) oxide reduction/oxidation in atmospheric pressure plasma jet, Electrochem Commun 95 (2018) 38–42. https://doi.org/10.1016/j.elecom.2018.08.014.

[26] M.E. Sener, R. Quesada-Cabrera, I.P. Parkin, D.J. Caruana, Facile formation of black titania films using an atmospheric-pressure plasma jet, Green Chemistry 24 (2022) 2499–2505. https://doi.org/10.1039/D1GC03646G.

[27] V.K. Patel, S. Bhowmik, Plasma Processing of Aluminum Alloys to Promote Adhesion: A Critical Review, REVIEWS OF ADHESION AND ADHESIVES 5 (2017) 79–104. https://doi.org/10.7569/RAA.2017.097303.

[28] F. Hong, S. Hodges, C. Myant, D.E. Boyle, Open5x: Accessible 5-axis 3D printing and conformal slicing, ArXiv2202.11426v2 (2022). https://doi.org/10.1145/3491101.3519782.

[29] F. Hong, B. Lampret, C. Myant, S. Hodges, D. Boyle, 5-axis multi-material 3D printing of curved electrical traces, Addit Manuf 70, 103546 (2023). https://doi.org/10.1016/J.ADDMA.2023.103546.

[30] C.A. Schneider, W.S. Rasband, K.W. Eliceiri, NIH Image to ImageJ: 25 years of image analysis, Nat Methods 9 (2012) 671–675. https://doi.org/10.1038/nmeth.2089.

[31] T. Kordova, A. Mareska, M.A.R.T.I.N.Havl. Mika, USE OF ATMOSPHERIC PRESSURE PLASMA TO IMPROVE THE ADHESIVE PROPERTIES OF GLASS AND POLYAMIDE 6 IN THE BONDING OF ADDITIONAL PARTS IN THE AUTOMOTIVE INDUSTRY, CERAMICS-SILIKATY 67 (2023) 334–347. https://doi.org/10.13168/cs.2023.0034.

[32] Y. Li, H. Liu, Q. Bai, L. Lu, R. Zhang Peng and Shen, X. Yuan, X. Miao, W. Han, C. Yao, Atomistic investigation on interfacial properties of glass surfaces modeling plasma modification and the influence of wettability conditions on adhesion, Int J Adhes Adhes 122 (2023). https://doi.org/10.1016/j.ijadhadh.2023.103330.

[33] G.S. Settles, M.J. Hargather, A review of recent developments in schlieren and shadowgraph techniques, Meas Sci Technol 28 042001 (2017). https://doi.org/10.1088/1361-6501/AA5748.

[34] Y. Morabit, R.D. Whalley, E. Robert, M.I. Hasan, J.L. Walsh, Turbulence and entrainment in an atmospheric pressure dielectric barrier plasma jet, Plasma Processes and Polymers 17 (2020) 1900217. https://doi.org/10.1002/PPAP.201900217.

**Declaration of interests**

☐The authors declare that they have no known competing financial interests or personal relationships that could have appeared to influence the work reported in this paper.

☒The authors declare the following financial interests/personal relationships which may be considered as potential competing interests:

Daren Caruana reports financial support was provided by Engineering and Physical Sciences Research Council. Daren Caruana reports financial support was provided by Defence Science and Technology Laboratory. If there are other authors, they declare that they have no known competing financial interests or personal relationships that could have appeared to influence the work reported in this paper.

# Additive Metal Printing on Multi Materials using an Atmospheric Pressure Plasma Jet on a 5-Axis Platform

Oliver S. J. Hagger[a], Michael A. Parkes[a], Francis Lockwood Estrin[a], Stefanos Agrotis[a,b], Ivan P. Parkin[a], Albertus D. Handoko[b] and Daren J. Caruana*[a]

*a Department of Chemistry, Christopher Ingold laboratories, 20 Gordon St., London, WC1H 0AJ.*

*b Institute of Materials Research and Engineering (IMRE), Agency for Science, Technology and Research (A*STAR), 2 Fusionopolis Way, Innovis #08-03, Singapore 138634, Republic of Singapore*

Highlights:

- Atmospheric pressure helium gas plasma jet used to write silver metal tracks.
- Mounted plasma jet print head on to an in house constructed a 5-axis platform.
- Able to print pure metal on a range of materials from glass, ceramic and aluminium.
- Sustainable manufacturing using little primary resources.
- Aqueous metal salts as precursor used as a metal source.